Available online at www.sciencedirect.com
SCIENCE DIRECT®
Journal of Sound and Vibration 273 (2004) 249–276
JOURNAL OF SOUND AND VIBRATION
www.elsevier.com/locate/jsvi

Simulation of dynamics of beam structures with bolted joints using adjusted Iwan beam elements

Y. Song[a], C.J. Hartwigsen[b,1], D.M. McFarland[a], A.F. Vakakis[b,c], L.A. Bergman[a,*]

[a] *Department of Aeronautical and Astronautical Engineering, University of Illinois at Urbana-Champaign, 104 S. Wright St., 321E Talbot Lab. MC-236, Urbana, IL 61801, USA*
[b] *Department of Mechanical and Industrial Engineering, University of Illinois at Urbana-Champaign, Urbana, IL 61801, USA*
[c] *Division of Mechanics, National Technical University of Athens, GR-157 10 Zografos, Athens, Greece*

Received 20 May 2002; accepted 15 April 2003

Abstract

Mechanical joints often affect structural response, causing localized non-linear stiffness and damping changes. As many structures are assemblies, incorporating the effects of joints is necessary to produce predictive finite element models. In this paper, we present an adjusted Iwan beam element (AIBE) for dynamic response analysis of beam structures containing joints. The adjusted Iwan model consists of a combination of springs and frictional sliders that exhibits non-linear behavior due to the stick–slip characteristic of the latter. The beam element developed is two-dimensional and consists of two adjusted Iwan models and maintains the usual complement of degrees of freedom: transverse displacement and rotation at each of the two nodes. The resulting element includes six parameters, which must be determined. To circumvent the difficulty arising from the non-linear nature of the inverse problem, a multi-layer feed-forward neural network (MLFF) is employed to extract joint parameters from measured structural acceleration responses. A parameter identification procedure is implemented on a beam structure with a bolted joint. In this procedure, acceleration responses at one location on the beam structure due to one known impulsive forcing function are simulated for sets of combinations of varying joint parameters. A MLFF is developed and trained using the patterns of envelope data corresponding to these acceleration histories. The joint parameters are identified through the trained MLFF applied to the measured acceleration response. Then, using the identified joint parameters, acceleration responses of the jointed beam due to a different impulsive forcing function are predicted. The validity of the identified joint parameters is assessed by comparing simulated acceleration responses with experimental measurements.

*Corresponding author. Tel.: +1-217-333-4970; fax: +1-217-244-0720.
E-mail address: lbergman@uiuc.edu (L.A. Bergman).
[1] Currently at Sandia National Laboratories, Albuquerque, NM.

doi:10.1016/S0022-460X(03)00499-1

The capability of the AIBE to capture the effects of bolted joints on the dynamic responses of beam structures, and the efficacy of the MLFF parameter identification procedure, are demonstrated.

1. Introduction

Mechanical joints can have a significant effect on the dynamics of structures that contain them. Bolted or riveted joints cause local stiffness and damping changes and are often the primary source of energy dissipation and damping in assembled structures. In many such structures, damping due to relative interfacial joint motion can account for as much as 90% of the total [1]. Thus, accurate prediction of dynamic response of assembled structures to external excitation often hinges on efficacious modelling of the effect of the joint on structural behavior.

Considerable effort has being expended attempting to characterize the non-linear behavior of structures containing joints. Crawley and Aubert [2] proposed an experimental technique called "force-state mapping" to identify structural elements such as joints containing strong non-linearities, in which the force transmission properties of an element were measured as a function of its mechanical states. Wang and Sas [3] presented a method for identifying optimal linear joint stiffness and damping parameters from measured modal parameters (resonant frequency and damping ratio). Ren and Beards [4] used experimental frequency response data to extract optimal linear joint parameters, and Ren et al. [5] developed a general purpose technique based on multi-harmonic balance (MHB) to identify the properties of non-linear joints from dynamic test data. Liu and Ewins [6] presented a "more general and more practical" method to extract the "effective" mass, stiffness and damping parameters of a joint element from measured frequency response functions. Note that a common characteristic of all of the above is that no parametric model of the joint is required.

Researchers have long been interested in developing predictive dynamic parametric models of mechanical joints for reliable structural response analysis. The successful modelling of joints depends on understanding and reproducing the basic physics associated with a jointed interface. Various studies have identified micro- and macro-slip occurring along the interface as the source of change of interface stiffness and energy dissipation, which constitutes the hysteresis mechanism of joints. Typically, the normal interface pressure across a dynamically loaded joint is not uniformly distributed, and micro-slip first occurs in regions where the contact pressure is insufficient to prevent it. The interface is, thus, divided into zones of "stick" and "slip". As the magnitude of the transmitted load increases, slip zones enlarge and coalesce, resulting in macro-slip and the familiar hysteretic force–displacement joint characteristic. This has been demonstrated experimentally for shear lap joints, loaded axially and torsionally, by Gaul and Lenz [7].

The notion that the non-linear hysteresis behavior of a joint is the result of micro- and macro-slip occurring along its interface was motivation for developing detailed finite element joint models, which requires solving a contact problem at the interface using an extremely fine mesh. While it is possible to realistically model the behavior of the joint in this manner, the resulting

joint model is impractical for dynamic analysis of an arbitrary structure containing the joint. In fact, it is computationally prohibitive and likely to remain so for some time [8]. Lee et al. [9] proposed a technique to reduce the number of degrees of freedom of a detailed finite element contact model. Chen and Deng [10] noted that finite element analysis can provide a flexible and reliable tool for understanding and characterizing the non-linear damping behavior of structural joints and proposed to use the finite element method to generate numerical data for a typical slip joint.

A lumped-parameter model of small dimension to simulate the non-linear dynamic behavior of a joint and, particularly, its effect upon the surrounding structure has long been deemed desirable. It has been common to represent the friction occurring at contact interfaces by a Coulomb friction model [11–14]. However, a single Coulomb friction element is only capable of describing either the full slip or full stick situation. Menq et al. [15,16] developed a one-dimensional, physically motivated micro-slip model that allows partial slip on the friction interface; however, this model is not suited to response analysis of complex structures. At present, non-linear, reduced order, full-joint models that can be effectively used in structural dynamic response analysis do not exist [8].

In this paper, we present the so-called adjusted Iwan beam element (AIBE) to simulate the non-linear effects of a bolted joint on beam structures. Iwan [17,18] used parallel–series and series–parallel spring–slider models to describe the hysteretic behavior of materials and structures. The series–parallel formulation leads to a constitutive relation in the form of strain as a function of stress, while the parallel–series formulation leads to stress as a function of strain, which makes it favorable for our analysis. Thus, we will only discuss the parallel–series model. Iwan's models, which are networks of springs and frictional sliders, reasonably simulate joint behavior since the observed hysteresis is achieved through stick–slip behavior of the sliders. An experimental investigation by Gaul and Lenz [7] demonstrated that the one-dimensional behavior of a lap joint can be represented by an adjusted Iwan model; this will be illustrated in a later section.

The adjusted Iwan beam element proposed herein consists of two adjusted Iwan models leading to the usual arrangement of degrees of freedom in the two-dimensional beam element: transverse displacement and rotation at each of the two nodes. Three parameters are required to characterize each adjusted Iwan model, which must be determined initially. The parameter identification constitutes an inverse problem, and a multi-layer feed-forward neural network (MLFF) is employed to extract joint parameters from measured structural acceleration response data.

The parameter identification procedure was implemented for a beam structure containing a bolted joint. Acceleration responses to a known impulsive forcing function at a fixed location on the beam were simulated for sets of combinations of joint parameters. A MLFF was developed and trained using envelope data from aforementioned acceleration time histories. Specific joint parameters were then identified using the trained MLFF on the measured acceleration response. Then, using the identified joint parameters, acceleration responses of the jointed beam due to another different impulsive forcing function were predicted. The efficacy of the AIBE and our parameter identification procedure were validated through comparisons of numerical and experimental acceleration responses to two different impulsive forcing functions at various points throughout the structure.

2. The adjusted Iwan model

2.1. Iwan's parallel–series model

The parallel–series model of Fig. 1 comprises a series of Jenkins elements. Each Jenkins element consists of a linear spring with elastic stiffness k/N in series with a Coulomb slider with critical slipping force f_i^*/N $(i = 1, 2, \ldots, N)$. The Jenkins element is an ideal elasto-plastic unit. Fig. 2 shows its force–deformation characteristic.

Let the number of Jenkins elements $N \to \infty$, and let f_i^* be defined in terms of a distribution function $\varphi(f^*)$; then $\varphi(f^*)\,\mathrm{d}f^*$ is the fraction of elements having a critical slipping force between f^* and $f^* + \mathrm{d}f^*$. The force–displacement hysteresis loop associated with the parallel–series combination can then be obtained by analyzing groups of Jenkins elements under varying stick–slip conditions. Here, we express it conveniently as

$$f = f(k, x, \hbar_x, \varphi(f^*)), \tag{1}$$

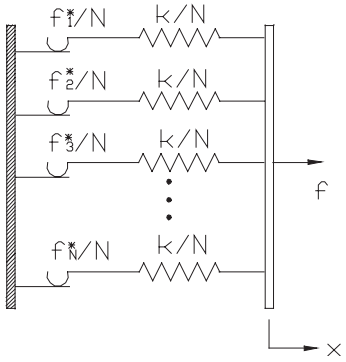

Fig. 1. Iwan's one-dimensional parallel–series model.

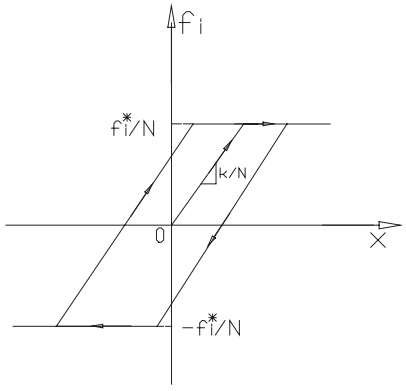

Fig. 2. Force–deformation relation of a single Jenkins element.

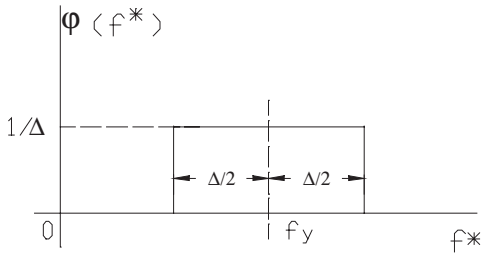

Fig. 3. Distribution function of critical slipping force $\varphi(f^*)$.

where x is the extension of the elements and $\hbar_x$ is the displacement history. When all of the Jenkins elements slip, the system reaches its ultimate force

$$f_y = \int_0^\infty f^* \varphi(f^*)\, \mathrm{d}f^*. \tag{2}$$

The distribution function of critical slipping force $\varphi(f^*)$ can take a number of forms. Following Iwan [17], we choose $\varphi(f^*)$ to be a band-limited function centered about f_y with width Δ and unit area, as shown in Fig. 3. Defining the coefficient

$$\beta = \frac{\Delta}{2f_y}, \tag{3}$$

the distribution function $\varphi(f^*)$ can be described as

$$\begin{cases} \varphi(f^*) = \dfrac{1}{2\beta f_y}, & f_y(1-\beta) \leqslant f^* \leqslant f_y(1+\beta), \\ \varphi(f^*) = 0, & \text{otherwise.} \end{cases} \tag{4}$$

2.2. Adjusted Iwan model

The ultimate force f_y indicates the onset of macro-slip. In Iwan's model, the stiffness of the system becomes zero after the force reaches f_y, which contradicts the experimental observation by Gaul and Lenz [7] that a joint possesses some stiffness even during macro-slip. To address this discrepancy, we add an additional linear elastic spring k_a in parallel with the Iwan model as shown in Fig. 4. The stiffness of the additional spring is that of the system at the onset of macro-slip. The ratio of spring coefficients is then defined to be

$$\alpha = \frac{k_a}{k}. \tag{5}$$

The corresponding force–displacement relation of the adjusted Iwan model can be obtained by changing the original stiffness k to $k - k_a$ and adding $k_a x$ to the original force–displacement relation in (1); i.e.,

$$f_{adjusted} = f(k - k_a, x, \hbar_x, \varphi(f^*)) + k_a x. \tag{6}$$

Typical hysteresis loops of an Iwan parallel–series model ($\alpha = 0.0$) and an adjusted Iwan model ($\alpha = 0.167$), in terms of a transient deformation history shown in Fig. 5, are depicted in Figs. 6(a)

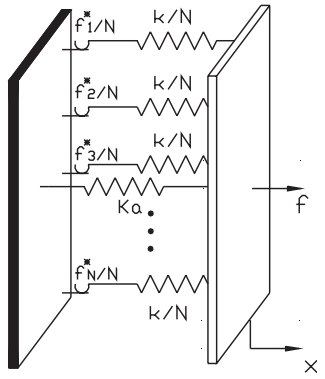

Fig. 4. Adjusted Iwan model.

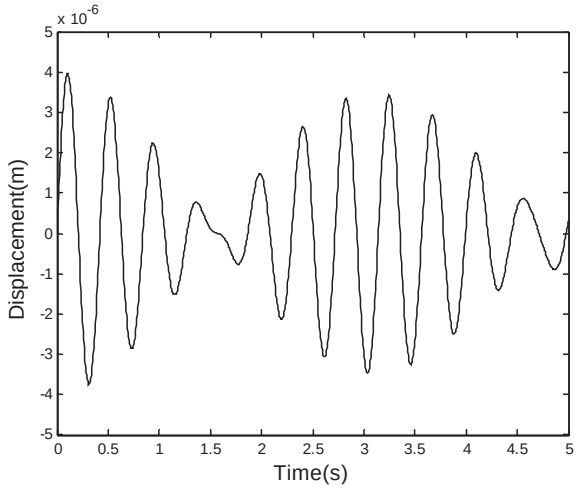

Fig. 5. The deformation history corresponding to the hysteresis loops of Fig. 6.

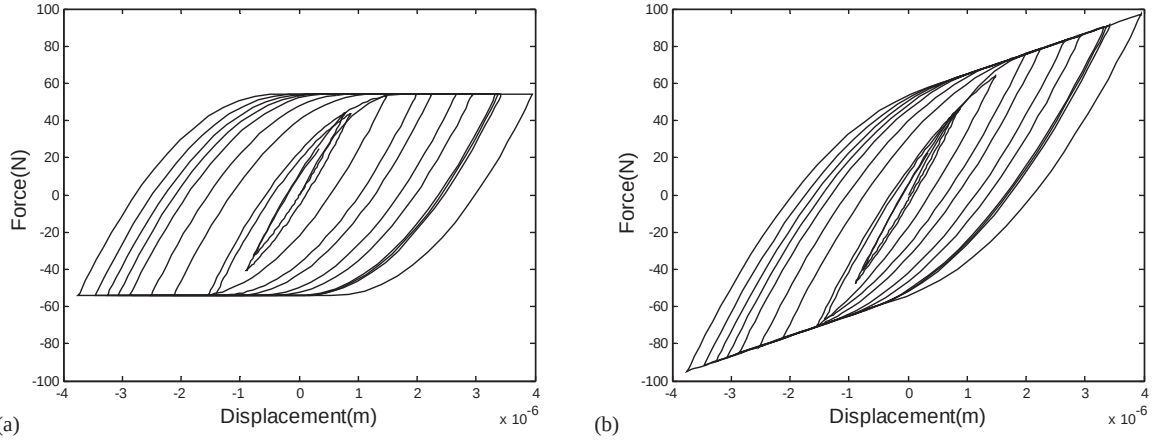

Fig. 6. Typical hysteresis loops in terms of the deformation history shown in Fig. 5. (a) Iwan's parallel–series model. (b) Adjusted Iwan model.

and (b), respectively. Other parameters of the models used are $\beta = 1.0$, $f_y = 54$ N, and $k = 6.5255 \times 10^7$ N/m. The hysteresis loop of the adjusted Iwan model appears similar to the loops obtained experimentally by Gaul and Lenz [7].

3. The adjusted Iwan beam element (AIBE)

3.1. Linear elastic beam element

The linear elastic beam element can be reduced to rigid bars and two springs with constant stiffnesses k_1 and k_2, as shown in Fig. 7, where h and L are the fixed height and length of the element, respectively. There are one translational and one rotational degree of freedom at each end of the element; i.e., w_i and θ_i $(i = 1, 2)$. The corresponding shear forces and bending moments are Q_1, Q_2 and M_1, M_2, respectively. The extensional deformations of the two springs are given by

$$\Delta_1 = \frac{L}{2}(\theta_1 + \theta_2) + (w_1 - w_2), \quad \Delta_2 = \frac{h}{2}(\theta_1 - \theta_2), \tag{7a, b}$$

which cause internal linear elastic forces in the springs

$$f_1 = k_1 \Delta_1, \quad f_2 = k_2 \Delta_2. \tag{8a, b}$$

The shear forces and bending moments at the two ends of the element are due to the internal spring forces f_1 and f_2. They are related by

$$Q_1 = f_1, \quad M_1 = \frac{L}{2} f_1 + \frac{h}{2} f_2, \tag{9a, b}$$

$$Q_2 = -f_1, \quad M_2 = \frac{L}{2} f_1 - \frac{h}{2} f_2. \tag{9c, d}$$

Choosing the stiffnesses of the two springs to be

$$k_1 = 12\frac{EI}{L^3}, \quad k_2 = 4\frac{EI}{Lh^2}, \tag{10a, b}$$

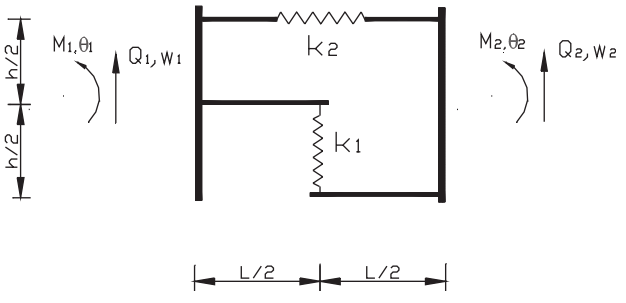

Fig. 7. Linear elastic beam element.

in which EI is the bending stiffness of the beam, and substituting Eqs. (7), (8) and (10) into Eq. (9), we obtain

$$\begin{Bmatrix} Q_1 \\ M_1 \\ Q_2 \\ M_2 \end{Bmatrix} = \frac{EI}{L} \begin{bmatrix} \frac{12}{L^2} & \frac{6}{L} & -\frac{12}{L^2} & \frac{6}{L} \\ \frac{6}{L} & 4 & -\frac{6}{L} & 2 \\ -\frac{12}{L^2} & -\frac{6}{L} & \frac{12}{L^2} & -\frac{6}{L} \\ \frac{6}{L} & 2 & -\frac{6}{L} & 4 \end{bmatrix} \begin{Bmatrix} w_1 \\ \theta_1 \\ w_2 \\ \theta_2 \end{Bmatrix}. \tag{11}$$

Clearly, the force–displacement relation for the element given by Eq. (11) is equivalent to that of the two-dimensional FE beam element.

3.2. Adjusted Iwan beam element

The adjusted Iwan beam element (AIBE) is obtained by replacing the two springs in the linear elastic element shown in Section 3.1 with two one-dimensional adjusted Iwan models, as shown in Fig. 8. For the adjusted Iwan beam element, Eqs. (7) and (9) remain valid. However, the internal forces f_1 and f_2 become functions of the deformation histories associated with the two adjusted Iwan models,

$$Q_1 = f_1(\Delta_1, \hbar_1), \quad M_1 = \frac{L}{2} f_1(\Delta_1, \hbar_1) + \frac{h}{2} f_2(\Delta_2, \hbar_2), \tag{12a, b}$$

$$Q_2 = -f_1(\Delta_1, \hbar_1), \quad M_2 = \frac{L}{2} f_1(\Delta_1, \hbar_1) - \frac{h}{2} f_2(\Delta_2, \hbar_2), \tag{12c, d}$$

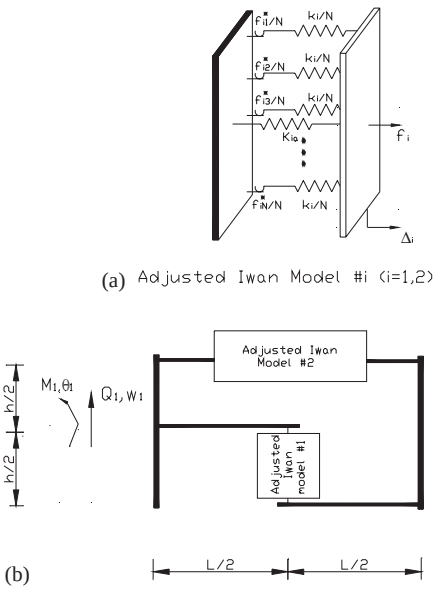

Fig. 8. (a) Adjusted Iwan model ($i = 1, 2$). (b) Adjusted Iwan beam element.

in which $\Delta_1 = (L/2)(\theta_1 + \theta_2) + (w_1 - w_2)$ and $\Delta_2 = (h/2)(\theta_1 - \theta_2)$; $\hbar_1$ and $\hbar_2$ represent the deformation histories of Δ_1 and Δ_2, respectively. The hysteresis loops associated with f_1 and f_2 can be determined as long as the distribution functions $\varphi_1(f_1^*)$ and $\varphi_2(f_2^*)$ for the two adjusted Iwan models are given. Here we will use the same band-limited function as in Section 2.1; thus, there are three parameters that must be identified for each adjusted Iwan element: the distribution coefficients β_i, ultimate forces f_{yi}, and stiffness ratios α_i $(i = 1, 2)$. Parameter identification will be discussed in Section 5.

4. Dynamic response analysis of jointed beam structures

In this analysis, adjusted Iwan beam elements are employed to represent the joints, and the remainder of the structure is represented by linear elastic beam elements. We assume that the numbers of linear elastic beam elements and adjusted Iwan beam elements are n and m, respectively. For the ith elastic beam element $(i = 1, 2, \ldots, n)$, the equations of motion in local co-ordinates are

$$\mathbf{f}^e_{elastic\ i} + \mathbf{f}^e_{internal\ i} = \mathbf{M}^e_i \ddot{\mathbf{d}}^e_i + \mathbf{K}^e_i \mathbf{d}^e_i \tag{13a}$$

$$\mathbf{d}^e_i = \{w_1,\ \theta_1,\ w_2,\ \theta_2\}^{\mathrm{T}}_i, \quad \mathbf{f}^e_{elastic\ i} = \{Q_1,\ M_1,\ Q_2,\ M_2\}^{\mathrm{T}}_i, \tag{13b, c}$$

in which $\mathbf{M}^e_i$ and $\mathbf{K}^e_i$ are element mass and stiffness matrices; $\mathbf{f}^e_{elastic\ i}$ is the element external force vector; $\mathbf{f}^e_{internal\ i}$ is the element internal force vector due to adjoining elements; and $\mathbf{d}^e_i$ is nodal displacement vector. For the ith adjusted Iwan beam element $(i = 1, 2, \ldots, m)$, the element equations of motion in local co-ordinates are

$$\mathbf{f}^e_{AIBE\ i} + \mathbf{f}^e_{internal\ i} = \mathbf{M}^e_i \ddot{\mathbf{d}}^e_i + \mathbf{f}^e_{s\ i} = \mathbf{M}^e_i \ddot{\mathbf{d}}^e_i + \left\{ \begin{array}{c} f_1(\Delta_1, \hbar_1) \\ \dfrac{L}{2} f_1(\Delta_1, \hbar_1) + \dfrac{h}{2} f_2(\Delta_2, \hbar_2) \\ -f_1(\Delta_1, \hbar_1) \\ \dfrac{L}{2} f_1(\Delta_1, \hbar_1) - \dfrac{h}{2} f_2(\Delta_2, \hbar_2) \end{array} \right\}_i, \tag{14}$$

where $\mathbf{M}^e_i$ is presumed the same as that for the elastic beam element in Eq. (13a); $\mathbf{f}^e_{s\ i}$ is the internal element nodal force vector due to deformation; and $\mathbf{f}^e_{AIBE\ i}$ is the element external force vector.

The equations of motion of the system are obtained by considering force equilibrium at each node. Note that the summation of element internal force vectors $\mathbf{f}^e_{internal\ i}$ $(i = 1, 2, \ldots, n + m)$ always equals zero. If the total number of degrees of freedom in the structure is n^d, then the assembly of n equations of motion for the linear elastic beam elements with m equations of motion for the adjusted Iwan beam elements in global co-ordinates gives

$$(\mathbf{M}^{elastic} + \mathbf{M}^{AIBE})\ddot{\mathbf{d}} + \mathbf{K}^{elastic}\mathbf{d} + \mathbf{F}_s(\mathbf{d}) = \mathbf{F}_{external}, \tag{15}$$

in which

$$\mathbf{M}^{elastic} = \sum_{i=1}^{n} \mathbf{G}_i^{\mathrm{T}} \bar{\mathbf{M}}^e_i \mathbf{G}_i, \quad \bar{\mathbf{M}}^e_i = \mathbf{T}^{\mathrm{T}} \mathbf{M}^e_i \mathbf{T}, \tag{16a}$$

$$\mathbf{M}^{AIBE} = \sum_{i=1}^{m} \tilde{\mathbf{G}}_i^{\mathrm{T}} \bar{\mathbf{M}}_i^e \tilde{\mathbf{G}}_i, \quad \bar{\mathbf{M}}_i^e = \mathbf{T}^{\mathrm{T}} \mathbf{M}_i^e \mathbf{T}, \tag{16b}$$

$$\mathbf{K}^{elastic} = \sum_{i=1}^{n} \mathbf{G}_i^{\mathrm{T}} \bar{\mathbf{K}}_i^e \mathbf{G}_i, \quad \bar{\mathbf{K}}_i^e = \mathbf{T}^{\mathrm{T}} \mathbf{K}_i^e \mathbf{T}, \tag{16c}$$

$$\mathbf{F}_s = \sum_{i=1}^{m} \tilde{\mathbf{G}}_i^{\mathrm{T}} \bar{\mathbf{f}}_{s\,i}^e, \quad \bar{\mathbf{f}}_{s\,i}^e = \mathbf{T}^{\mathrm{T}} \mathbf{f}_{s\,i}^e, \tag{16d}$$

$$\mathbf{F}_{external} = \sum_{i=1}^{n} \mathbf{G}_i^{\mathrm{T}} \bar{\mathbf{f}}_{elastic\,i}^e + \sum_{i=1}^{m} \tilde{\mathbf{G}}_i^{\mathrm{T}} \bar{\mathbf{f}}_{AIBE\,i}^e, \quad \bar{\mathbf{f}}_{elastic\,i}^e = \mathbf{T}^{\mathrm{T}} \mathbf{f}_{elastic\,i}^e, \quad \bar{\mathbf{f}}_{AIBE\,i}^e = \mathbf{T}^{\mathrm{T}} \mathbf{f}_{AIBE\,i}^e. \tag{16e}$$

Here, $\mathbf{G}_i$ and $\tilde{\mathbf{G}}_i$ are the Kronecker matrices reflecting the connectivity information of the ith linear elastic beam element and adjusted Iwan beam element, respectively, and $\mathbf{T}$ is the co-ordinate transformation matrix. The dimensions of $\tilde{\mathbf{G}}_i$ and $\mathbf{G}_i$ are $4 \times n^d$, since every beam element contains four degrees of freedom. The dimensions of $\mathbf{M}^{elastic}$, $\mathbf{M}^{AIBE}$, $\mathbf{K}^{elastic}$ are $n^d \times n^d$ and the dimensions of $\mathbf{F}_s$ and $\mathbf{F}_{external}$ are $n^d \times 1$.

The formulae above do not include terms related to material damping, which plays an important role in system response. In our analysis, material damping is addressed in the same way as in linear response analysis. For example, if Rayleigh damping is considered, we simply add a damping term to Eq. (15) to get

$$(\mathbf{M}^{elastic} + \mathbf{M}^{AIBE})\ddot{\mathbf{d}} + \mathbf{C}\dot{\mathbf{d}} + \mathbf{K}^{elastic}\mathbf{d} + \mathbf{F}_s(\mathbf{d}) = \mathbf{F}_{external}, \tag{17}$$

where

$$\mathbf{C} = \bar{\alpha}(\mathbf{M}^{elastic} + \mathbf{M}^{AIBE}) + \bar{\beta}(\mathbf{K}^{elastic} + \mathbf{K}_e^{AIBE}). \tag{18}$$

Here, $\mathbf{K}_e^{AIBE}$ is the contribution of the joint stiffness to the system when all joints are modelled by linear elastic beam elements, and $\bar{\alpha}$, $\bar{\beta}$ are Rayleigh damping coefficients.

The dynamic response of the system can be obtained by directly integrating the non-linear equations of motion (17). An explicit formulation, the forward incremental displacement central difference method [19], is employed in our analysis. In this scheme, the unknown response at future time is explicitly computed in terms of known responses up to and including the present time. Since no equilibrium iterations are required, the explicit formulation is very efficient for solving non-linear equations of motion.

5. Parameter identification

5.1. Parameters of the adjusted Iwan beam elements

Determination of the parameters of the adjusted Iwan beam elements from the dynamic responses of the structure constitutes an inverse problem. The adjusted Iwan beam element, as presented, consists of two one-dimensional adjusted Iwan models. As noted earlier, six parameters

must be identified for each joint: the distribution coefficients β_i, ultimate forces f_{yi}, and stiffness ratios α_i $(i = 1, 2)$.

The distribution coefficient β_i controls the shape of the initial loading curves (in both positive and negative senses) and of the reloading/unloading curves prior to the occurrence of macro-slip in the hysteresis loops of the adjusted Iwan model; the ultimate force f_{yi} determines the force level at which macro-slip occurs; and the α_i provides the stiffness of the adjusted Iwan model after macro-slip. The area enclosed by a single hysteresis loop represents the energy dissipated during a cycle of deformation. Comparatively, both f_{yi} and α_i have a greater effect on the enclosed area of the hysteresis loop and resulting energy dissipation than the distribution coefficient β_i.

To enhance the efficiency of the identification procedure, we assume that the two adjusted Iwan models in the adjusted Iwan beam element share the same parameters, and we set the distribution coefficient β_i to 1.0. The choice of $\beta_i = 1.0$ ensures that the distribution function of critical slipping force has a non-zero value $1/(2f_{yi})$ in the range $[0, 2f_{yi}]$; i.e., micro-slip will occur in the joint interface even at very low forcing levels, which is consistent with experimental observations [20]. Thus, only two parameters of the original six remain to be identified. While this may seem to be somewhat constraining, retaining two free parameters is sufficient to represent the complicated behavior of the actual joint with the AIBE.

5.2. Neural networks in inverse problems

Parameter identification problems lack unique solution and are, thus, often formulated in an optimization framework in which the parameters of the assumed model are found within the predefined space of variables to minimize the difference between measured and computed responses in some norm. However, because of the highly non-linear nature of joint behavior, the application of classical optimization methods, many of which are gradient-based, to our inverse problem becomes problematic, and we resort to a "soft" method.

Soft computing encompasses a large class of (often) biologically inspired methods, including neural networks and genetic algorithms, which are frequently applied to inverse problems. These methods are model-free and robust to imprecision and uncertainty, making it possible to solve otherwise intractable problems [21,22]. A survey paper summarizing the application of neural networks to problems in computational mechanics was recently published by Yagawa and Okuda [23].

We have adopted the multi-layer feed-forward (MLFF) neural network for our inverse problem [21,24–27]. Neural networks are massively parallel computational models. Through training, neural networks learn and generalize complex relations and associations between input and output data. The trained neural networks are then capable of estimating output given new input according to the mapping or association resulting from the training procedure. Fig. 9 shows a typical MLFF with bias, consisting of four layers of neurons. The outer layers are input and output; the intermediate layers are hidden. Neurons or nodes in each layer are fully connected to all nodes in the adjoining layers. Each neuron receives signals through its incoming connections, performs some simple operations (adding the received signals to the bias to get an input value, calculating the output value by applying a transfer function to the input value), and sends signals through its outgoing connections. The strength of each connection depends on its weight. Learning is a procedure in which the connection weights and biases are updated using a

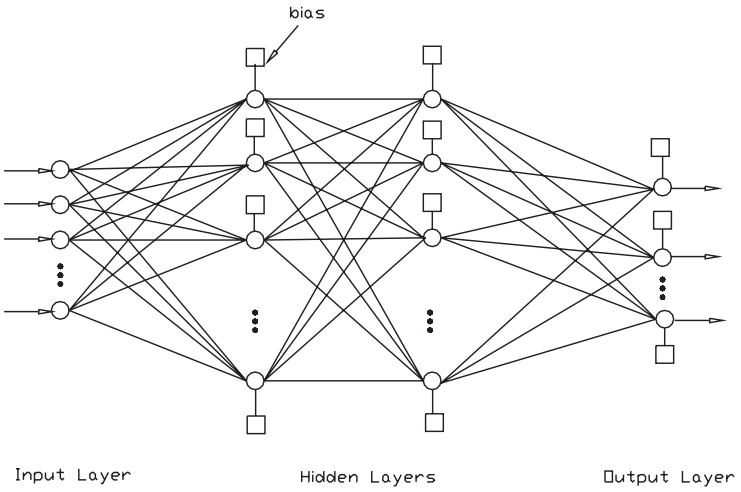

Fig. 9. A typical MLFF neural network with bias.

back-propagation training algorithm such that the given input produces the known corresponding output. The resulting knowledge is stored in the connection weights and biases [28].

The application of neural networks to inverse problems consists of three stages: (1) determination of the neural network architecture, (2) selection of training patterns, and (3) training. The three are interrelated and interactive. For the MLFF, error back-propagation is the most popular and efficient training algorithm [29]. Convergence of error back-propagation is strongly affected by the neural network architecture and the quality and quantity of selected training patterns [30]. The quality and quantity of training patterns also have strong influence on the generalization capability of the neural network, and application of some kind of regularization of the input and output data before training has become standard practice [31]. With respect to network architecture, the number of nodes in the input and output layers corresponds to the number of elements of input and output, respectively. However, there is no rigorous method for selecting the appropriate numbers of hidden layers and neurons, although the automatic node generation of neural networks has been studied [32]. Trial and error is still the most widely used method in practical applications.

The learning capability of a neural network depends on the number of hidden layers and the number of nodes in each. If the size of the neural network is too small compared to the complexity of the mapping between input and output data, the training procedure can be slow to converge, or the neural network can fall into a local minimum. On the other hand, if the neural network is too large, the training time increases dramatically, and the likelihood of over-fitting, in which case the neural network produces very accurate output upon input of training samples but gives large errors when subjected to a new input set, increases.

5.3. A parameter identification procedure by MLFF neural net

For a linear viscously damped structure, the envelope of free response for any mode decays exponentially with an exponent proportional to the modal damping. If the envelope is not

exponential, the damping is not purely linear viscous. In a jointed structure, dissipation occurs not only by viscous loss but also through micro- and macro-slip occurring in the joint interfaces. Changes in damping and stiffness at the joints are amplitude-dependent (thus, it is not reasonable to derive the "equivalent" modal damping from the decay envelope). For jointed structures, therefore, decay response is the best information we can use to gain insight into the damping, as with the decreasing of vibratory motion, the system damping (and stiffness) is changing continually with time, showing different properties at different vibration amplitudes. In our parameter identification procedure, we use envelopes of measured acceleration responses following impact excitations, which are readily obtained, to identify joint parameters associated with the adjusted Iwan beam elements. Our parameter identification procedure using the MLFF employs the following steps:

(1) A number of combinations of the two free joint parameters are predefined. For each combination, the dynamic response is determined by a direct finite element analysis.
(2) The upper envelope of the resulting acceleration time history at the beam location of interest is calculated and fitted by a polynomial. The polynomial is evaluated at predefined points in time producing discrete data from the envelope. This data and the model parameters are regularized producing a single training pattern. A set of training patterns are obtained for all the combinations in step (1).
(3) The MLFF neural network is implemented and trained using the above set of training patterns. The error back-propagation algorithm is employed. In each training pattern, the input is the envelope data from step (2), and the output is the predefined combination of the two joint parameters.
(4) System accelerations from laboratory experiments are then used to generate the corresponding envelope data. The same regularization scheme used in step (2) is applied to the experimental data.
(5) This data is applied to the trained MLFF to identify the model parameters corresponding to the experimental structure. This completes the inverse analysis.

6. Impulsive load experiments on beam structures

6.1. Test set-up and procedure

Two different beam configurations were prepared for impact hammer testing: a jointed beam, and a monolithic beam. The jointed beam structure, shown in Fig. 10, made of low-carbon steel, consists of a simple beam that incorporates a double shear lap joint in its center. When installed, the bolts were torqued to 6.22 N m, which provided sufficient clamping force to preserve the integrity of the beam while allowing for obvious hysteresis to take place. The monolithic beam structure was machined from a single piece of the same low-carbon steel. With bolts installed, it is identical to the jointed beam but without the lap joint interfaces. Thus, any differences seen in the dynamic response of the two structures are assumed to be caused by the joint.

To achieve a high degree of repeatability in the hammer tests, both beams were suspended from the ceiling by a nylon cord at each end to approximate free–free boundary conditions. The data

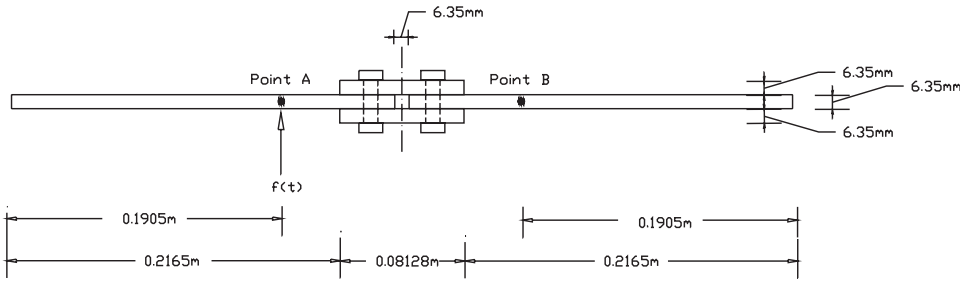

Fig. 10. The beam structure with one double lap joint.

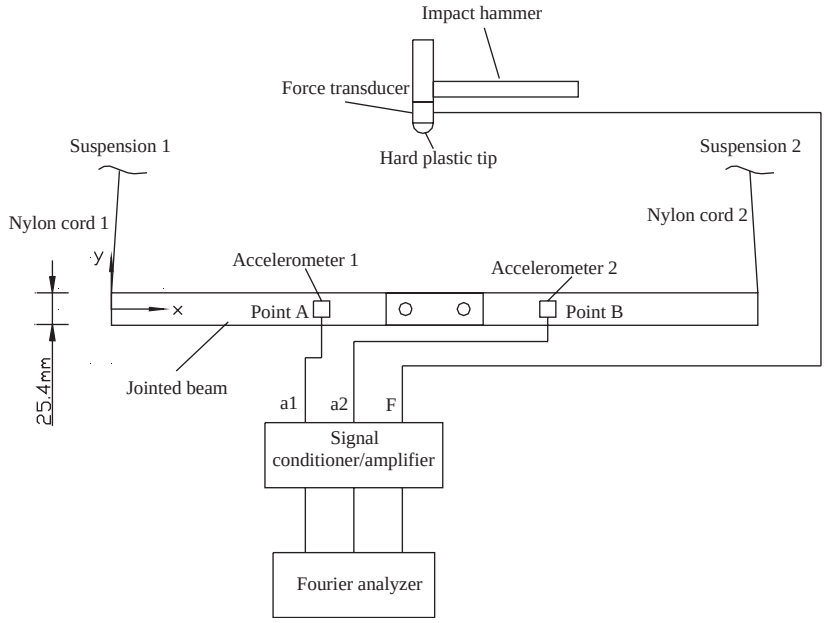

Fig. 11. Experimental set-up for impact hammer test.

acquisition system used in all tests is shown in Fig. 11. Input forces were measured by the integral force transducer mounted on the PCB Model 086C04 impact hammer, to which a hard plastic tip was attached. Accelerations were measured by PCB Model 356A11 miniature tri-axial accelerometers attached at points A and B on the beams. All input forces and output accelerations were applied or measured in the z-direction, as indicated in the figure.

An experimental modal analysis was performed for the monolithic beam in order to determine modal parameters and Rayleigh damping constants. The accelerometer was fastened to the beam at point A, and hammer excitation was applied at points along the beam to obtain the frequency response functions. The bandwidth of the Fourier analyzer, Tektronix Model 2630, was 2 kHz, allowing measurement of the first five modes of the beam. Natural frequencies and modal damping ratios were determined from the FRFs using Diamond software [33]. The modal

parameters were used to verify the FE model and to determine the linear damping matrix **C**, assumed identical for the monolithic and jointed beams.

A series of impulse response experiments was then completed for both the monolithic and jointed beams. The beams were struck by the instrumented hammer at point A. The input force and the acceleration response at points A and B were measured. For the monolithic beam a single forcing level, and for the jointed beam two different forcing levels, were used, and for both, a measurement bandwidth of 5 kHz was employed.

6.2. Experimental results

The first five natural frequencies and modal damping factors obtained from the monolithic beam are summarized in Table 1.

For the monolithic beam, Fig. 12 shows the measured input force, as well as the synthesized forcing function used for numerical simulation in Section 7.2. The measured accelerations at points A and B are shown in Fig. 13.

The two forcing levels employed in tests of the jointed beam are denoted *hard hit* and *soft hit*. Figs. 14 and 15 show the measured hard hit input force, along with the synthesized forcing function used for numerical simulation in Section 7.3, and resulting accelerations. Similar results for the soft hit are given in Figs. 16 and 17.

Table 1
Modal survey of the monolithic beam

	Mode				
	1st	2nd	3rd	4th	5th
Natural frequency (Hz)	139.0	341.3	758.0	1092.6	1962.6
Modal damping ratio (%)	0.12	0.06	0.04	0.03	0.02

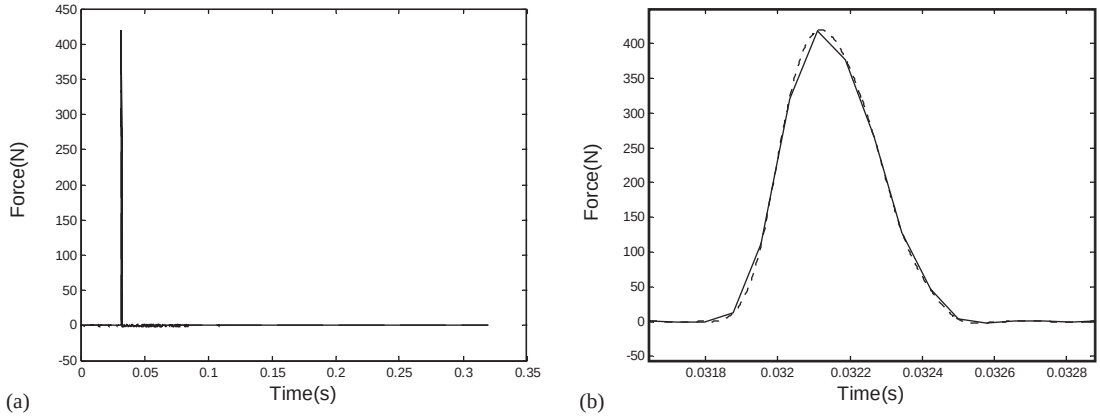

Fig. 12. Excitation of the monolithic beam: (a) Forcing functions. (b) A detailed view. ——, Measured forcing function; - - - - -, forcing function used in numerical simulation.

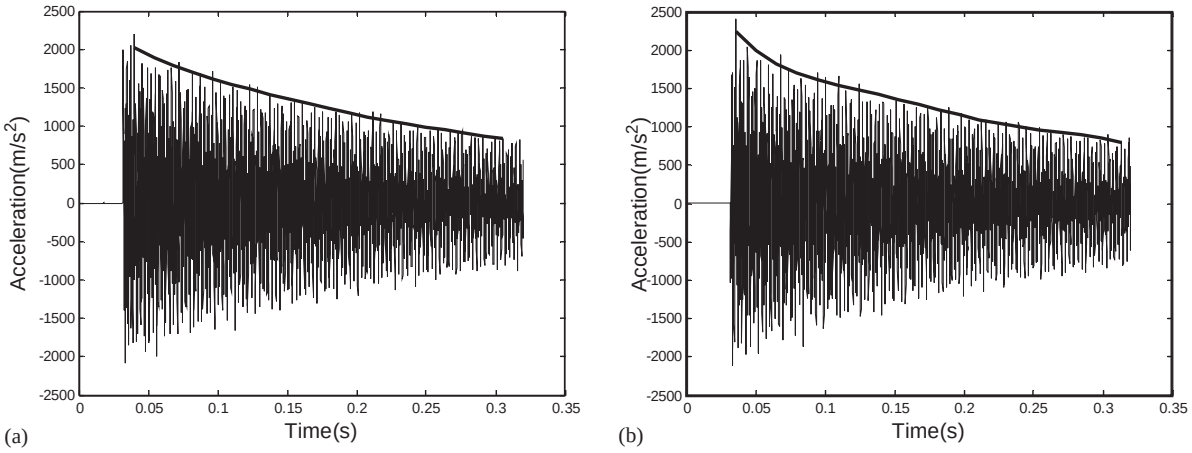

Fig. 13. Measured acceleration histories for the monolithic beam. (a) Point A. (b) Point B.

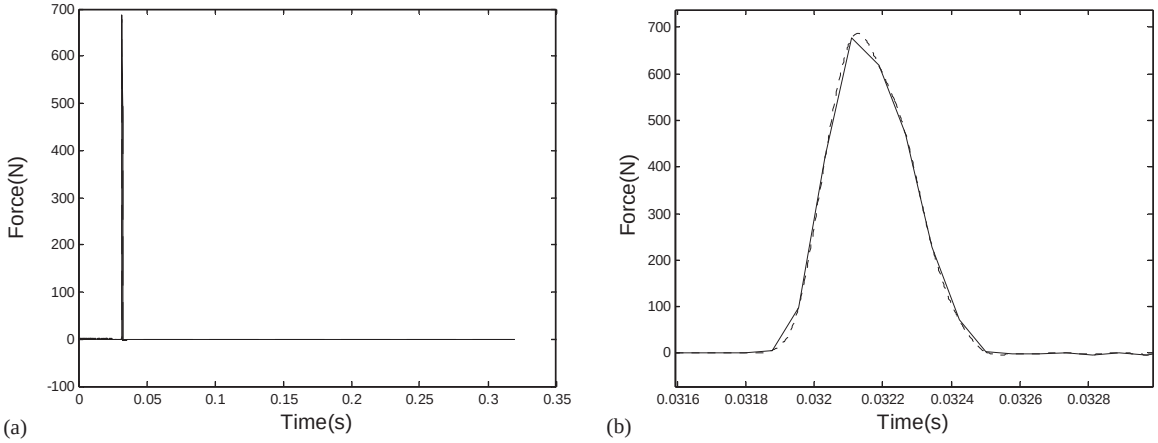

Fig. 14. Forcing functions for the jointed beam, hard hit test. (a) Forcing functions. (b) A detailed view. ——, Measured forcing function; - - - - -, forcing function used in numerical simulation.

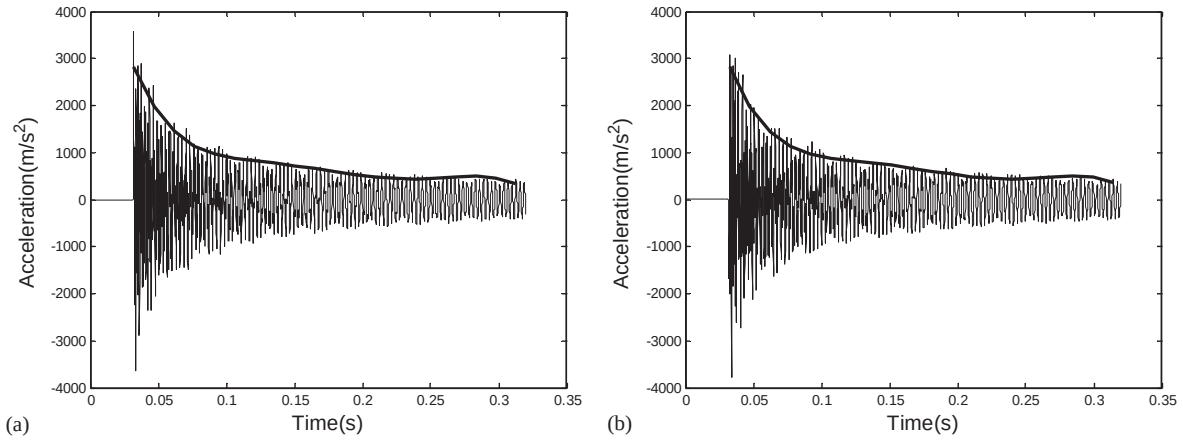

Fig. 15. Measured acceleration histories for the jointed beam, hard hit test. (a) Point A. (b) Point B.

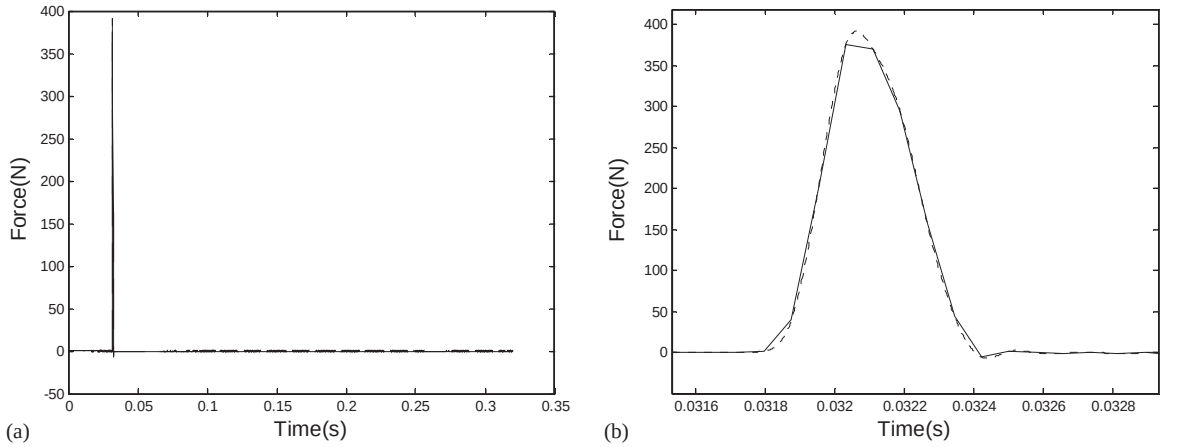

Fig. 16. Forcing functions for the jointed beam, soft hit test. (a) Forcing functions. (b) A detailed view. ——, Measured forcing function; - - - - -, forcing function used in numerical simulation.

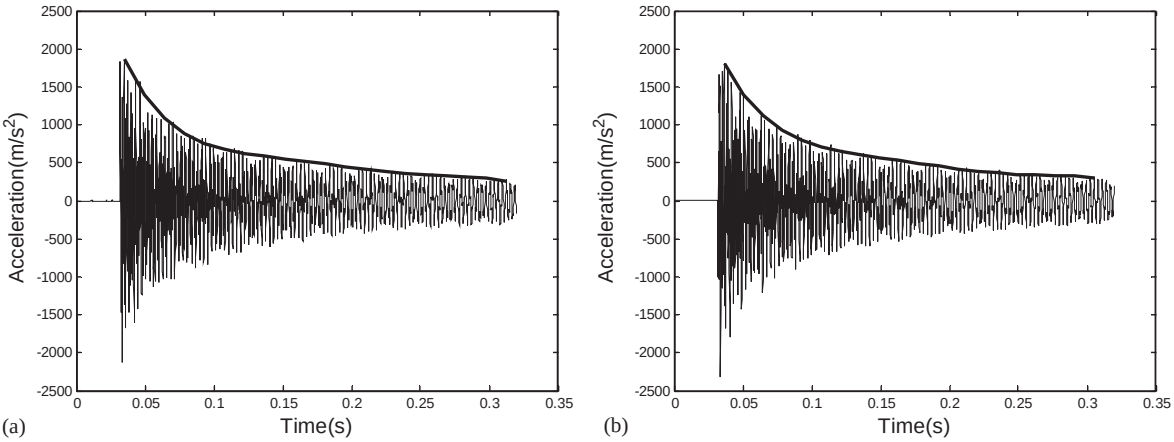

Fig. 17. Measured acceleration histories for the jointed beam, soft hit test. (a) Point A. (b) Point B.

Examination of Figs. 13, 15 and 17 illustrate the differences observed in acceleration response between the monolithic and jointed beams. The damping in the monolithic beam is known to be amplitude-independent. Clearly, the jointed beam is more highly damped than the monolithic beam. In the jointed beam, the impact causes a response that initially decays very rapidly (i.e., more damping) but then reverts to a decay rate similar to that of the monolithic beam once the level of vibration decreases sufficiently. The soft hit causes a response that appears more like the response of the monolithic beam than that of the hard hit, but still different. These observations can be explained by the behavior of the joint. At small amplitudes, the joint hysteresis loops are nearly straight lines enclosing little area, meaning that little energy is dissipated in each cycle. As the amplitude increases, the loops enclose more area, which implies increased energy dissipation.

7. Parameter identification of the jointed beam structure

7.1. Finite element models

Finite element models were developed to simulate the impulse response of both the monolithic and jointed beams, as shown in Fig. 18. The monolithic beam was discretized into nine linear elastic beam elements, while the jointed beam was represented by one adjusted Iwan beam element (element no. 5), and eight linear elastic beam elements. The dimensions and material properties of these elements are given in Table 2.

A numerical modal analysis was performed using the linear finite element model for the monolithic beam. The first five natural frequencies are compared in Table 3. The maximum error compared to the experimental data was found to be 1.36% in the fifth mode, a very good result.

7.2. Determination of the system damping matrix

Eq. (17) requires knowledge not only of the parameters of the joint but also the linear damping matrix **C**. Rayleigh damping is assumed; thus, the Rayleigh damping coefficients $\bar{\alpha}$ and $\bar{\beta}$ were

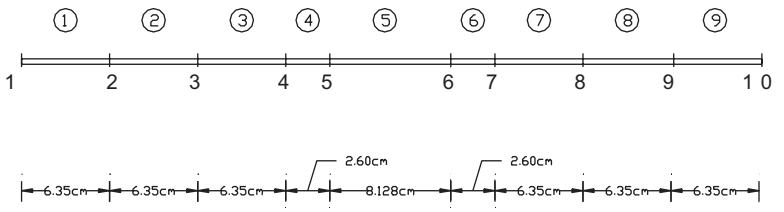

Fig. 18. Finite element mesh for the monolithic and jointed beams.

Table 2
Properties of the beam elements

	Elastic beam element	Adjusted Iwan beam element
Area of cross-section A (m^2)	1.61×10^{-4}	4.84×10^{-4}
Moment of inertia I (m^4)	5.42×10^{-10}	1.46×10^{-8}
Mass density ρ (kg/m^3)	7.95×10^{3}	7.95×10^{3}
Young's modulus E (Pa)	2.0×10^{11}	2.0×10^{11}

Table 3
Comparison of measured and computed natural frequencies for the monolithic beam

	Mode				
	1st	2nd	3rd	4th	5th
Measured natural frequency (Hz)	139.0	341.3	758.0	1092.6	1962.6
Computed natural frequency (Hz)	138.8	338.5	755.9	1099.4	1989.2
Error (%)	−0.14	−0.83	−0.28	+0.62	+1.36

determined. For the monolithic beam, the first two computed natural frequencies are

$$\omega_1 = 872.2 \text{ rad/s}, \quad \omega_2 = 2126.7 \text{ rad/s} \tag{19}$$

and the first two experimentally determined damping ratios are

$$\varsigma_1 = 0.0012, \quad \varsigma_2 = 0.0006, \tag{20}$$

from which

$$\bar{\alpha} = \frac{2\omega_1\omega_2(\varsigma_1\omega_2 - \varsigma_2\omega_1)}{\omega_2^2 - \omega_1^2} = 2.000 \text{ s}^{-1}, \tag{21a}$$

$$\bar{\beta} = \frac{2(\varsigma_2\omega_2 - \varsigma_1\omega_1)}{\omega_2^2 - \omega_1^2} = 1.220 \times 10^{-7} \text{ s}. \tag{21b}$$

For verification, a numerical simulation of the impact hammer test on the monolithic beam described in Section 6 was completed, using the derived damping matrix and forcing function in Fig. 12. The simulated acceleration histories, with their envelopes, are compared with experimental results in both time and frequency domains in Figs. 19 and 20, for points A and B, respectively. To determine the degree of agreement between the two, we introduce the normalized envelope error function (NEE),

$$\text{NEE}(t) = \left| \frac{f_{sim}(t) - f_{exp}(t)}{\max[f_{exp}(t)]} \right|, \tag{22}$$

where $f_{sim}(t)$ and $f_{exp}(t)$ are the simulated and experimental acceleration envelope functions, respectively and t represents time. For the envelopes at point A, examining 20 points, the largest NEE is 4.1% and the average NEE is 2.5%; at point B, the two numbers are 6.5% and 2.9%, respectively. The reasonable agreement between simulated and experimental acceleration envelopes demonstrates the validity of the damping matrix, which will be used in the analysis of the jointed beam. We note, however, that the computed accelerations are sensitive to $\bar{\alpha}$ and $\bar{\beta}$. In general, some model updating may be required to bring the computed and measured acceleration responses into agreement.

7.3. Parameter identification for the bolted joint

The parameters of the jointed beam can now be determined by using the acceleration at point A recorded during the hard hit test described in Section 6. Following this, the acceleration response of the jointed beam due to a soft hit is predicted using the previously identified parameters.

In the identification procedure, the MLFF with one hidden layer was developed; input data was the upper envelope of the hard hit acceleration time history of the jointed beam at point A. Since each envelope contains 25 points, the input layer of the MLFF has 25 neurons, and by our previous assumptions, just two adjusted Iwan beam element parameters will be identified: $f_{y1} = f_{y2}$ and $\alpha_1 = \alpha_2$. Thus, the output layer of the MLFF has two neurons. There are 10 neurons

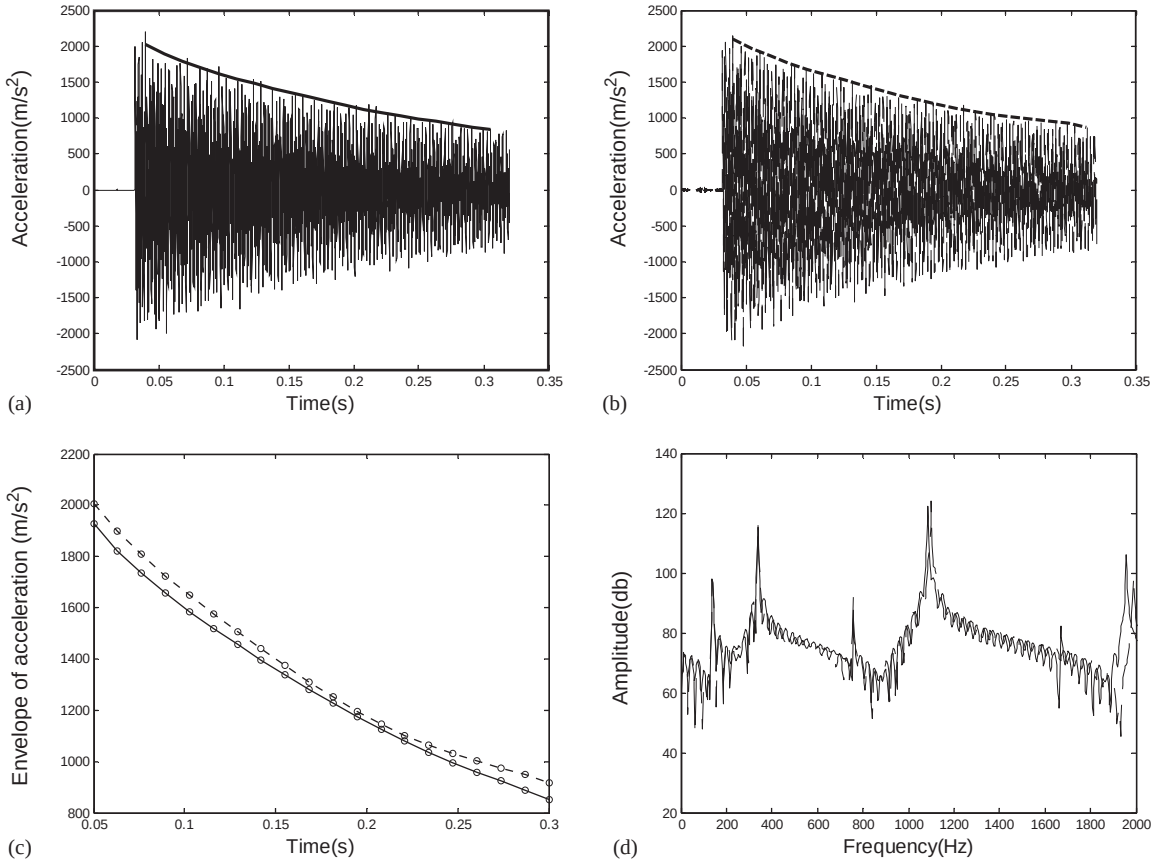

Fig. 19. Measured and simulated responses, at point A, for the monolithic beam. (a) Measured acceleration. (b) Simulated acceleration. (c) Envelopes of accelerations. (d) FFT of accelerations. ——, Measured results; - - - - -, simulated results.

in the hidden layer, and the transfer functions in the hidden and output layers are the hyperbolic tangent sigmoid function "tansig" and the hard limit function "purelin", respectively. They are defined as [34]

$$\text{tansig}(x) = \frac{2}{1+\mathrm{e}^{-2x}} - 1, \quad \text{purelin}(x) = x. \tag{23a, b}$$

The MLFF with bias is shown in Fig. 21. To train the MLFF, the response of the system to the forcing function measured in the hard hit test was determined by setting the ultimate forces f_{yi} to 30, 40, 50, 60, 70, 80 N and the stiffness ratio α_i to 0.1, 0.15, 0.2, 0.25, 0.3. These combinations of α_i and f_{yi} generated a total of 30 normalized acceleration records at point A, which led to the 30 envelopes used to train the MLFF. Fig. 22 shows all 30 regularized envelopes, as well as that obtained experimentally for the actual beam containing the joint. The measured envelope sits within the 30 samples, which indicates that the actual system parameters were within the given range of each parameter. Once the training procedure was completed, the experimentally obtained

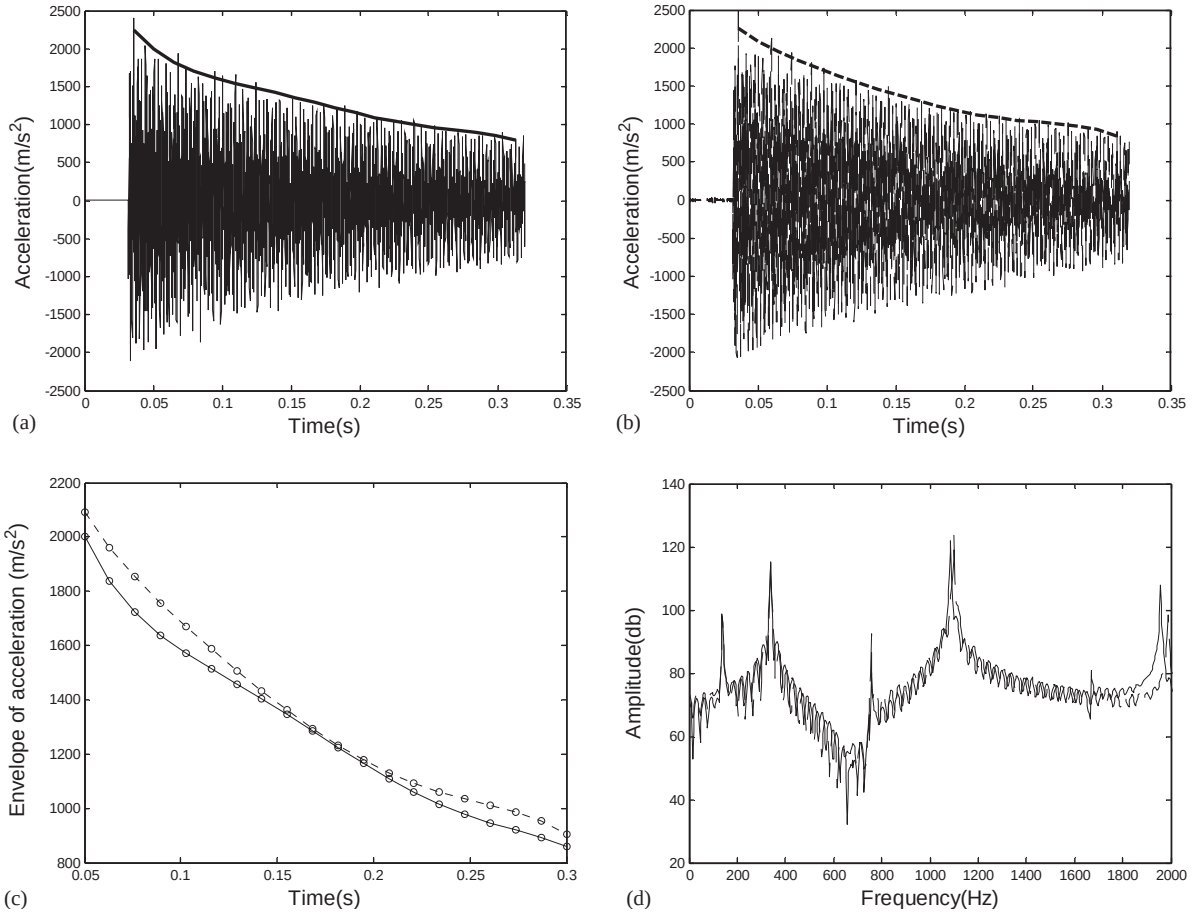

Fig. 20. Measured and simulated responses, at point B, for the monolithic beam. (a) Measured acceleration. (b) Simulated acceleration. (c) Envelopes of accelerations. (d) FFT of accelerations. ——, Measured results; - - - - -, simulated results.

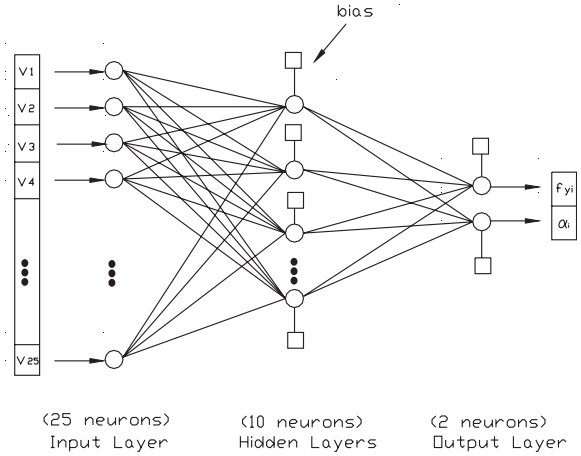

Fig. 21. The MLFF neural network with bias used in our problem.

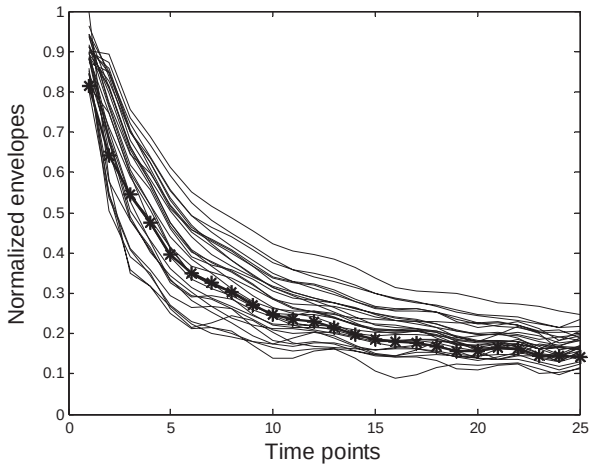

Fig. 22. The 30 training samples of envelopes and the experimentally obtained envelope (asterisk line) for the acceleration histories of the jointed beam at point A, hard hit test.

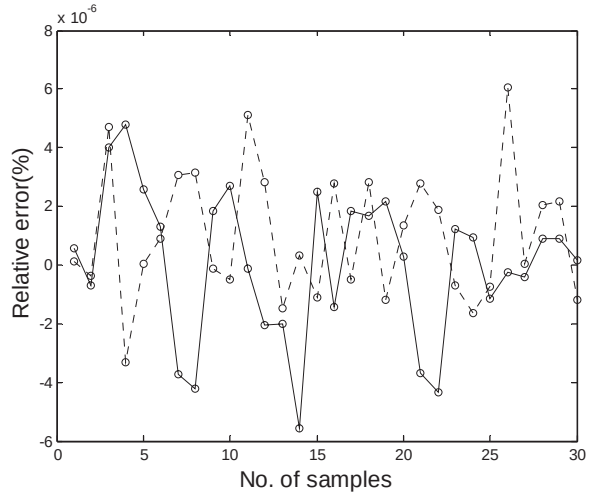

Fig. 23. The relative errors of samples after 250 epochs of training. ——, Ultimate force; - - - - -, stiffness ratio.

envelope of the acceleration time history at point A was applied to the MLFF to recover the joint parameters of the actual system.

An error back-propagation algorithm was used to train the MLFF in MATLAB. Fig. 23 shows the relative errors of the two parameters for the 30 samples after 250 training epochs. The trained MLFF gave the following values for the identified joint parameters:

$$f_{yi} = 54.3 \text{ N}, \quad \alpha_i = 0.167, \quad (i = 1, 2). \tag{24}$$

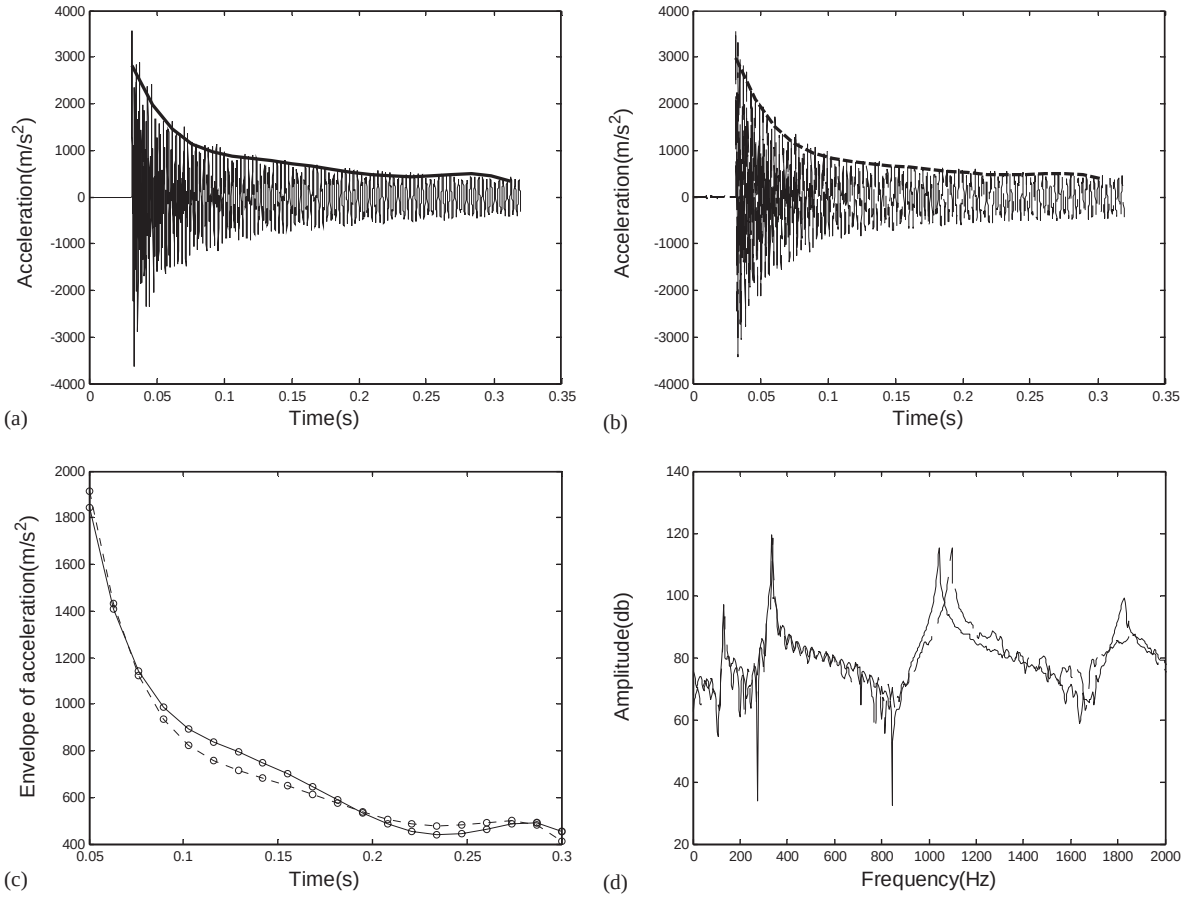

Fig. 24. Measured and simulated responses, at point A, for the jointed beam, hard hit test. (a) Measured acceleration. (b) Simulated acceleration. (c) Envelopes of accelerations. (d) FFT of accelerations. ——, Measured results; - - - - -, simulated results.

These parameters, along with $\beta_i = 1.0$, were used in the numerical simulation of the hard hit test. The simulated acceleration histories and their envelopes are compared with experimental results in both time and frequency domains in Figs. 24 and 25, for points A and B, respectively. The numerical results show good correspondence with experimental results. At point A, the largest NEE is 4.2% and the average NEE is 2.1%; at point B, the two numbers are 10.1% and 2.1%, respectively. Fig. 26 shows the computed hysteresis loops for the adjusted Iwan models 1 and 2 within the joint.

Applying these parameters to the soft hit test resulted in the comparisons of Figs. 27 and 28. Again, computational and experimental results agree fairly well. At point A, the largest NEE is 7.1% and the average NEE is 3.1%; at point B, the numbers are 10.1% and 4.1% , respectively. Fig. 29 shows the computed hysteresis loops for adjusted Iwan models 1 and 2 within the joint.

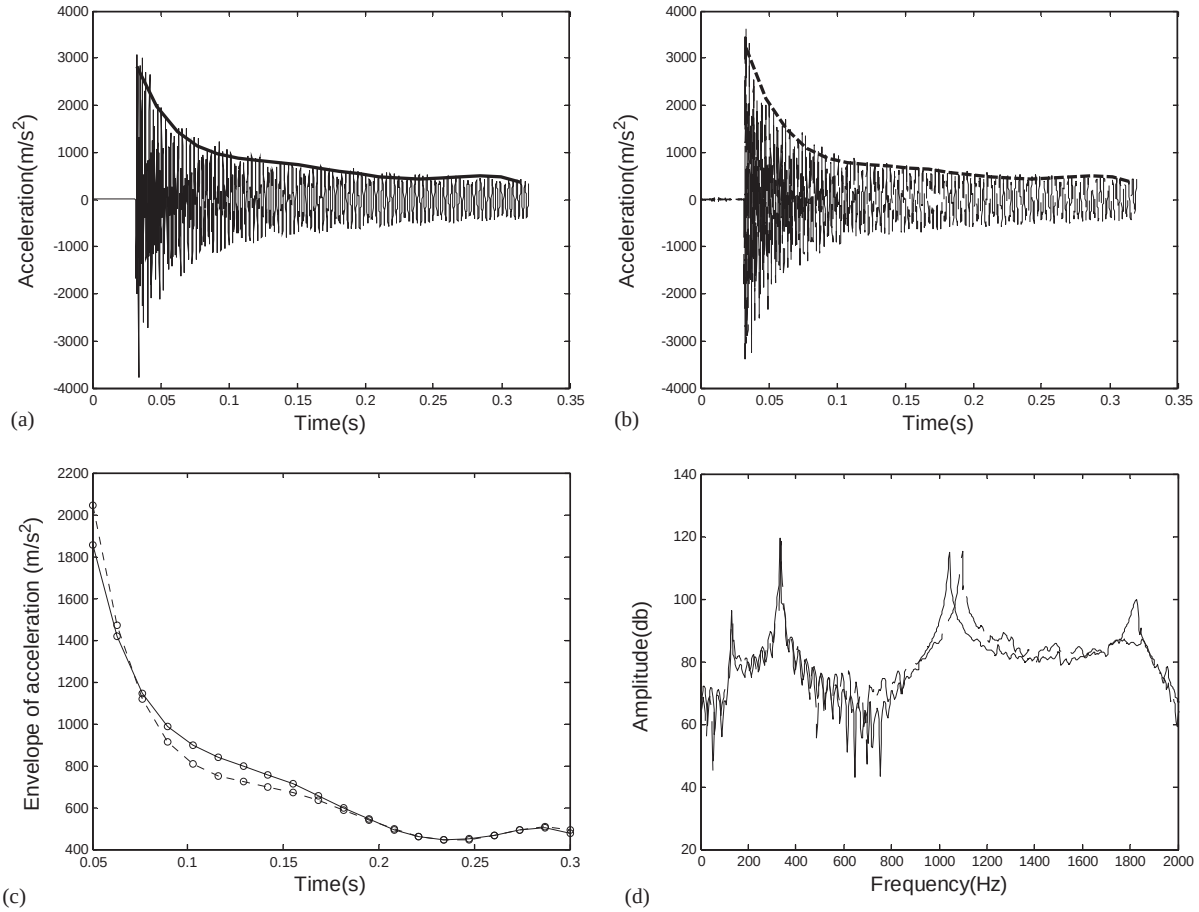

Fig. 25. Measured and simulated responses, at point B, for the jointed beam, hard hit test. (a) Measured acceleration. (b) Simulated acceleration. (c) Envelopes of accelerations. (d) FFT of accelerations. ——, Measured results; - - - - -, simulated results.

8. Conclusions

An adjusted Iwan beam element (AIBE) has been developed that simulates the non-linear dynamic behavior of bolted joints in beam structures. The element is compatible with the two-dimensional linear elastic beam finite element and is, thus, easily implemented.

A general method for non-linear dynamic analysis of beam structures with bolted joints is presented based upon use of the AIBE. Implementation requires initial determination of the parameters of each AIBE. For this, multi-layer feed-forward neural networks are employed to extract joint parameters from measured structural responses. The parameter identification procedure is applied to a beam structure with a single bolted joint. The comparison of numerical and experimental responses to two hammer tests under different forcing levels validates the capability of the model to capture the effects of bolted joints on the dynamic responses of beam

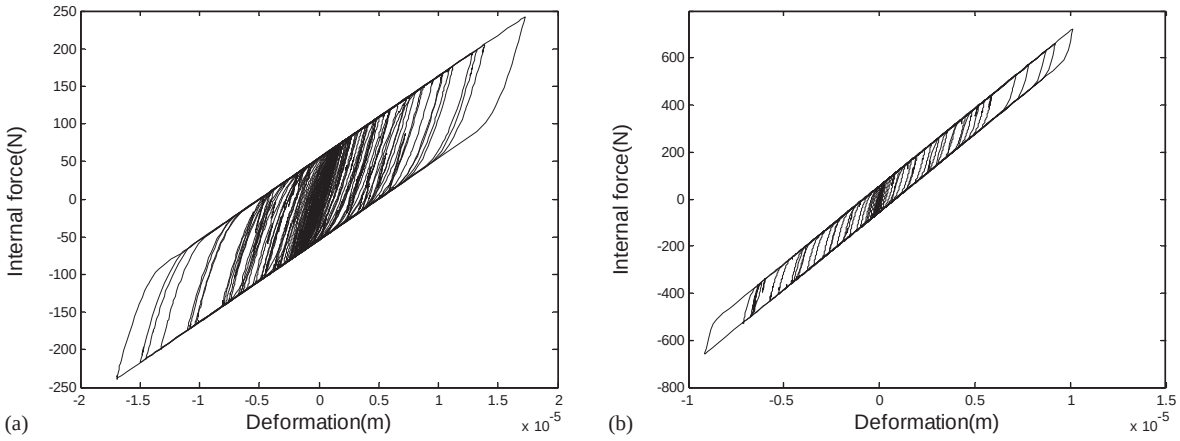

Fig. 26. Hysteresis loops, hard hit test. (a) Adjusted Iwan model no. 1. (b) Adjusted Iwan model no. 2.

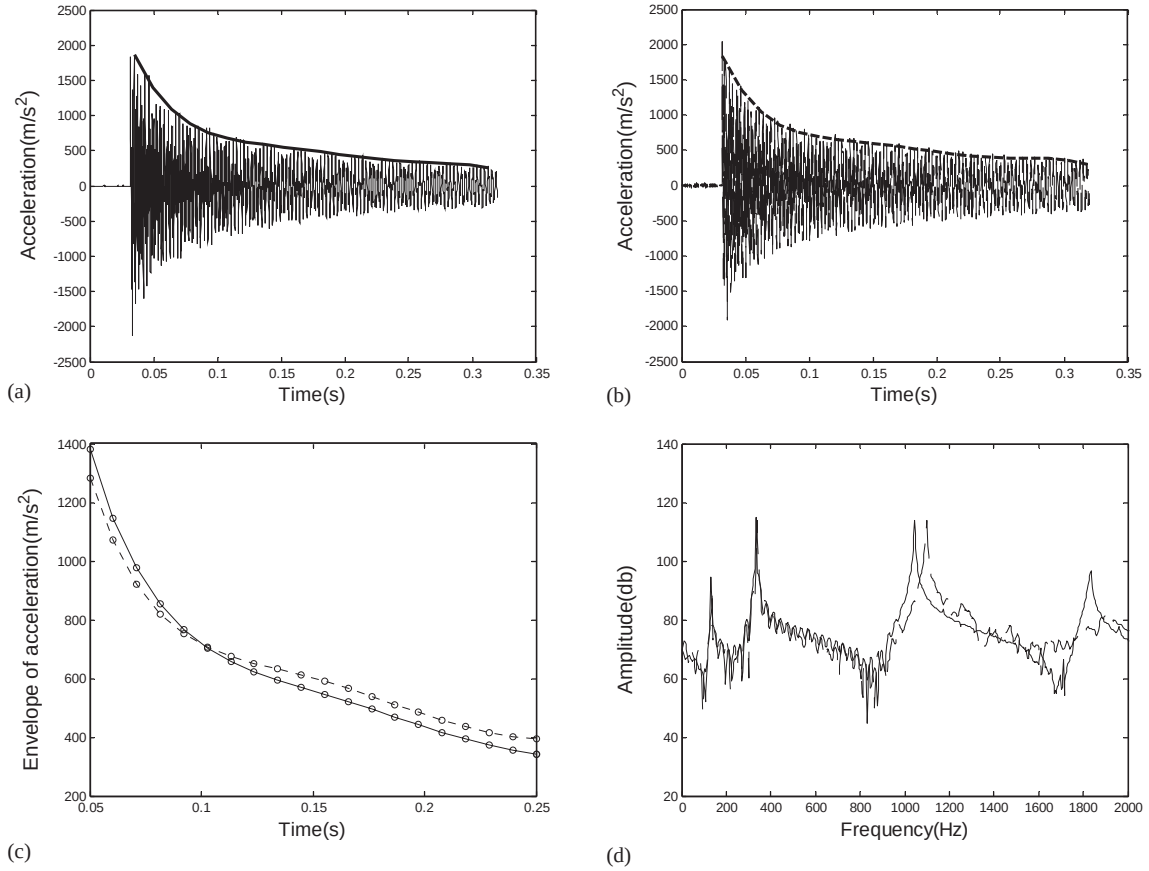

Fig. 27. Measured and simulated responses, at point A, for the jointed beam, soft hit test. (a) Measured acceleration. (b) Simulated acceleration. (c) Envelopes of accelerations. (d) FFT of accelerations. ——, Measured results; - - - - -, simulated results.

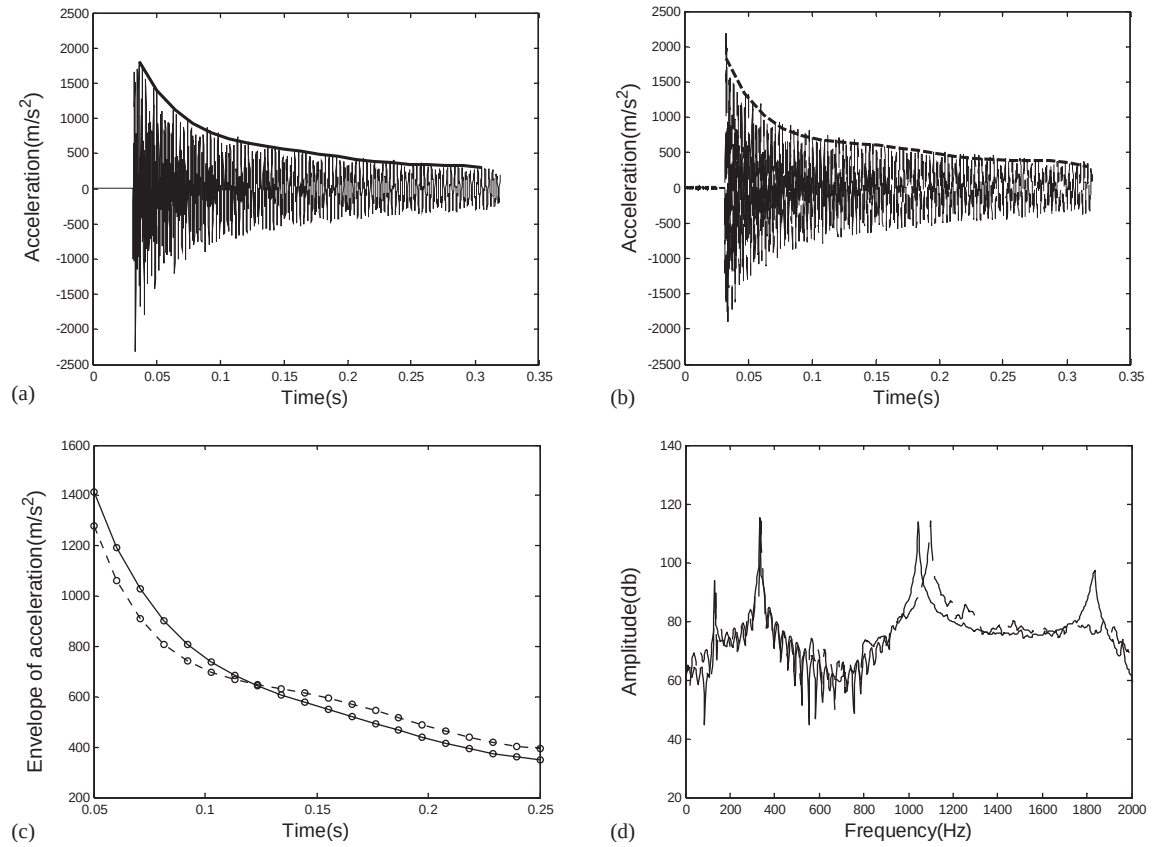

Fig. 28. Measured and simulated responses, at point B, for the jointed beam, soft hit test. (a) Measured acceleration. (b) Simulated acceleration. (c) Envelopes of accelerations. (d) FFT of accelerations. ——, Measured results; - - - - -, simulated results.

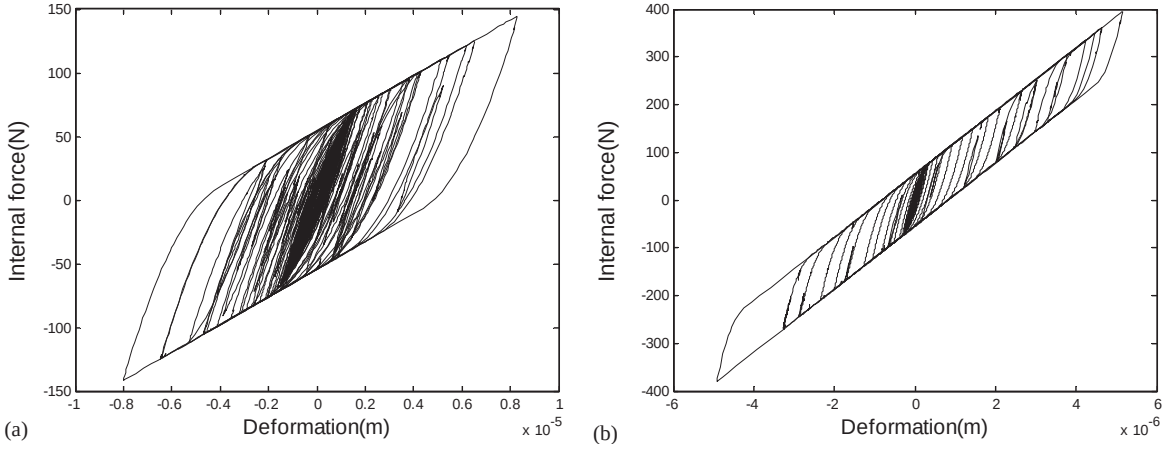

Fig. 29. Hysteresis loops, soft hit test. (a) Adjusted Iwan model no. 1. (b) Adjusted Iwan model no. 2.

structures, as well as the efficacy of the MLFF neural network parameter identification procedure to extract joint parameters.

Acknowledgements

This work was partially supported by Sandia National Laboratories through Contract Number DOE SNL BF-0162, Dr. Daniel Segalman, Project Director, and by the Office of Naval Research through Contract Number N00014-00-1-10187, Dr. Luise Couchman, Project Director.

References

[1] C.F. Beards, Damping in structural joints, *Shock and Vibration Digest* 24 (1992) 3–7.
[2] E.F. Crawley, A.C. Aubert, Identification of nonlinear structural elements by force-state mapping, *American Institute of Aeronautics and Astronautics Journal* 24 (1986) 155–162.
[3] J. Wang, P. Sas, A method for identifying parameters of mechanical joints, *American Society of Mechanical Engineers, Journal of Applied Mechanics* 57 (1990) 337–342.
[4] Y. Ren, C.F. Beards, Identification of "effective" linear joints using coupling and joint identification techniques, *American Society of Mechanical Engineers, Journal of Vibration and Acoustics* 120 (1998) 331–338.
[5] Y. Ren, T.M. Lim, M.K. Lim, Identification of properties of nonlinear joints using dynamic test data, *American Society of Mechanical Engineers, Journal of Vibration and Acoustics* 120 (1998) 324–330.
[6] W. Liu, D.J. Ewins, Substructure synthesis via elastic media part I: joint identification, *Proceedings of the 18th International Modal Analysis Conference*, San Antonio, 2000, pp. 1153–1159.
[7] L. Gaul, J. Lenz, Nonlinear dynamics of structures assembled by bolted joints, *Acta Mechanica* 125 (1997) 169–181.
[8] J.L. Dohner, D.L. Gregory, D. Segalman, D.R. Martinez, White paper: On the Development of Methodologies for Constructing Predictive Models of Structures with Joints and Interfaces, Structural Dynamics Department, Sandia National Laboratories, Albuquerque, NM, 2000.
[9] J.W. Lee, K.H. Ko, S. Lee, S.K. Kim, J.M. Lee, A dynamic analysis of complex structures with joints, *Proceedings of the 13th International Modal Analysis Conference*, Nashville, 1995, pp. 248–254.
[10] W. Chen, X. Deng, A finite element analysis of friction damping in a slip joint, *Proceedings of 1999 ASME Design Engineering Technical Conferences*, Las Vegas, DETC99/VIB-8189, 1999.
[11] C.-H. Menq, J.H. Griffin, A comparison of transient and steady state finite element analysis of the forced response of a frictionally damped beam, *American Society of Mechanical Engineers, Journal of Vibration, Acoustics, Stress, and Reliability in Design* 107 (1985) 19–25.
[12] S.W. Shaw, On the dynamic response of a system with dry friction, *Journal of Sound and Vibration* 108 (1986) 305–325.
[13] L. Gaul, S. Bohlen, Identification of nonlinear structural joint models and implementation in discretized structure models, *Proceedings of 11th ASME Conference on Mechanical Vibration and Noise*: *The Role of Damping in Vibration and Noise*, Boston, Vol. 5, 1987, pp. 213–219.
[14] A.A. Ferri, B.S. Heck, Vibration analysis of dry friction damped turbine blades using singular perturbation theory, *American Society of Mechanical Engineers, Journal of Vibration and Acoustics* 120 (1998) 588–595.
[15] C.-H. Menq, J. Bielak, J.H. Griffin, The influence of microslip on vibratory response, part I: a new microslip model, *Journal of Sound and Vibration* 107 (1986) 279–293.
[16] C.-H. Menq, J.H. Griffin, J. Bielak, The influence of microslip on vibratory response, part II: a comparison with experimental results, *Journal of Sound and Vibration* 107 (1986) 295–307.
[17] W.D. Iwan, A distributed-element model for hysteresis and its steady-state dynamic response, *American Society of Mechanical Engineers, Journal of Applied Mechanics* 33 (1966) 893–900.

[18] W.D. Iwan, On a class of models for the yielding behavior of continuous and composite systems, *American Society of Mechanical Engineers, Journal of Applied Mechanics* 34 (1967) 612–617.
[19] D. Sha, K.K. Tamma, M. Li, Robust explicit computational developments and solution strategies for impact problems involving friction, *International Journal for Numerical Methods in Engineering* 39 (1996) 721–739.
[20] J.D. Hinkle, L.D. Peterson, An experimental investigation of roughness-induced microslip in metallic interfaces, *40th SDM Conference*, AIAA-99-1382, St. Louis, MO, April 12–14, 1999.
[21] J. Ghaboussi, X. Wu, Soft computing with neural networks for engineering applications: fundamental issues and adaptive approaches, *Structural Engineering and Mechanics* 6 (1998) 955–969.
[22] J. Ghaboussi, Biologically inspired soft computing methods in structural mechanics and engineering, *Structural Engineering and Mechanics* 11 (2001) 485–502.
[23] G. Yagawa, H. Okuda, Neural networks in computational mechanics, *Archives of Computational Methods in Engineering* 3,4 (1996) 435–512.
[24] R.C. Eberhart, R.W. Dobbins, *Neural Network PC Tools: A Practical Guide*, Academic Press, New York, 1990.
[25] J.E. Dayhoff, *Neural Networks Architecture: An Introduction*, Van Nostrand Reinhold, New York, 1990.
[26] J.A. Freeman, D.M. Skapura, *Neural Networks: Algorithms, Applications, and Programming Techniques*, Addison-Wesley, Reading, MA, 1991.
[27] L. Tarassenko, *A Guide to Neural Computing Applications*, Wiley, New York, 1998.
[28] P.C. Pandey, S.V. Barai, Multilayer perception in damage detection of bridge structures, *Computers & Structures* 54 (1995) 597–608.
[29] S.V. Barai, P.C. Pandey, Performance of the generalized delta rule in structural damage detection, *Engineering Application of Artificial Intelligence* 8 (1995) 211–221.
[30] I.A. Basheer, Selection of methodology for neural network modeling of constitutive hysteresis behavior of soils, *Computer-Aided Civil and Infrastructure Engineering* 15 (2000) 440–458.
[31] S. Yoshimura, A. Matsuda, G. Yagawa, New regularization by transformation for neural network based inverse analyses and its application to structural identification, *International Journal for Numerical Methods in Engineering* 39 (1996) 3953–3968.
[32] A. Joghataie, J. Ghaboussi, X. Wu, Learning and architecture determination through automatic node generation, *Proceeding of the International Conference of Artificial Neural Networks in Engineering*, *ANNIE'95*, St. Louis, 1995, pp. 45–50.
[33] S.W. Doebling, C.R. Farrar, P.J. Cornwell, DIAMOND: a graphical user interface toolbox for comparative modal analysis and damage identification, *Proceeding of the Sixth International Conference on Recent Advances in Structural Dynamics*, Southampton, UK, 1997, pp. 399–412.
[34] D. Howard, M. Beale, *Neural Network Toolbox, for Use with MATLAB*, *User's Guide*, *Version* 4, The MathWorks, Inc., Natick, MA, 2000.